Nanoscale

PAPER

View Article Online
View Journal

Cite this: DOI: 10.1039/d4nr01489h

Rational design of dual-ion doped cobalt-free Li-rich cathode materials for enhanced cycle stability of lithium-ion pouch cell batteries†

Otavio Augusto Titton Dias, *‡[a] Farnaz Azarnia,‡[b] Keerti Rathi,[a] Viktoriya Pakharenko,[a] Vijay K. Tomer [a] and Mohini Sain[a]

The synergistic effect of single-crystal structure and dual doping in Li-rich cobalt-free cathode materials was thoroughly investigated. Lithium-ion pouch cells employing Sb/Sn doped $Li_{1.2}Mn_{0.6}Ni_{0.2}O_2$ and graphite exhibited a specific capacity of 191.01 mA h g^{-1} at 1C rate and exceptionally stable performance upon cycling, with capacity retention of 87.24% of their initial capacity after 250 cycles at 1C rate. The strategic combination of morphology manipulation and dual ion doping has markedly diminished cation mixing and expanded the Li interstitial sites within the cathode lattice. This work offers significant insights into the mechanisms responsible for the structural decline of Li-rich cobalt-free cathodes, emphasizing the importance of stabilizing the cathode lattice structure at high potential. These findings suggest promising potential for this material to meet the demanding energy density criteria for electric vehicles. Finally, this research provides practical strategies for effectively implementing high-voltage cobalt-free cathodes, offering valuable guidance for future applications.

Received 5th April 2024,
Accepted 6th July 2024

DOI: 10.1039/d4nr01489h

rsc.li/nanoscale

Introduction

Electric vehicles have emerged as a promising solution for mitigating greenhouse gas emissions and reducing reliance on fossil fuels within the transportation industry.[1–3] However, meeting the energy demands of electric cars requires materials with high specific energy to reduce the weight of battery components.[4,5] Simultaneously, it is crucial to utilize active materials that minimize the costs associated with metal extraction and production.[6] At the forefront of the widespread adoption of electric vehicles lies the advancement of high-capacity lithium-ion batteries (LIBs) characterized by enhanced energy density, reduced cost, and improved sustainability.[7] However, the reliance on cobalt (Co) in LIB cathodes poses significant challenges due to its high cost, limited availability, and ethical issues surrounding its mining practices.[8]

Achieving a balance between low cost, excellent cycling performance, and high energy density is crucial for electric vehicle batteries. Traditional cathode materials such as $LiCoO_2$, $LiMn_2O_4$, and $LiFePO_4$ often fail to meet these demands due to their low capacity or discharge voltage.[9,10] Consequently, there is a pressing need to develop high-voltage positive electrodes with high specific capacity to meet the requirements of advanced lithium-ion batteries (LIBs).[9] Recently, layered Li-rich cathodes have garnered significant attention owing to their impressive discharge capacity at a high working voltage of up to 4.8 V.[11] Despite these advantages, Li-rich materials suffer from low capacity and poor cycling performance, especially at high rates, limiting their practical application.[12] As is well known, cobalt's crucial role in maintaining rate capability, structural stability, and reducing cation mixing in Li-rich cathodes has proven challenging to replicate.[13] Additionally, cobalt-free cathode materials have been explored, but barriers remain in achieving the required energy density and long-term cycling stability, especially at higher voltages.[14] Given that the cost of batteries heavily depends on cathode materials, there is a growing interest in developing low-cobalt cathodes using earth-abundant elements as a desirable option. This approach aims to reduce costs while improving battery performance, thus driving the advancement of LIB technology.[9]

As reported in previous studies,[15–17] practical application faces significant hurdles, including notable initial irreversible capacity loss due to the simultaneous release of Li^+ and O^{2-} from the Li_2MnO_3 phase upon charging above 4.5 V, leading to low initial coulombic efficiency (ICE),[18] migration issues for Li/transition metal ions and triggering irreversible structural

[a]Department of Mechanical and Industrial Engineering, University of Toronto, Toronto, Ontario, Canada M5S 3G8. E-mail: otavio.dias@mail.utoronto.ca
[b]Centre for Biocomposites and Biomaterials Processing, John H. Daniels Faculty of Architecture, Landscape, and Design, University of Toronto, Toronto, Ontario, Canada M5S 3B3

†Electronic supplementary information (ESI) available. See DOI: https://doi.org/10.1039/d4nr01489h

‡These authors contributed equally to this work.

transformation from layered to spinel,[19] resulting in substantial capacity and voltage decay during prolonged cycling and limited rate capability attributed to low electronic/ionic conductivities.[20] Thus, imperative measures are required to stabilize the host crystal structure and mitigate microstructural defects to enhance performance for commercial applications.[21] Top of Form Various strategies have been adopted to improve the performance of Li-rich layered oxides, including surface modification,[22] bulk doping, converting into nanostructures, and exploring different synthesis routes.[23,24] To address these challenges, atom doping is a prominent method to improve battery stability and capacity in high voltages. Atom doping entails substituting atoms within the crystal lattice,[25] such as at nickel, cobalt, and manganese sites, with stable dopants like calcium,[26] magnesium,[27] aluminium,[28] titanium,[29] zirconium,[30] vanadium,[31] and niobium.[32] Introducing these elements reinforces the material's structural integrity, mitigating the impacts of thermal expansion and contraction and alleviating the stress caused by phase transitions during lithiation and delithiation.[33]

In this study, we focus on stabilizing Li-rich cobalt-free cathodes at a higher voltage of 4.8 V by doping them with elements such as antimony (Sb) and tin (Sn) to tailor their properties and enhance their performance for EV applications. In addition, our research endeavors to capitalize on these inherent advantages of single crystals to address the challenges associated with Li-rich cobalt-free cathodes. By synthesizing lithium-rich materials with a single crystal morphology, we aim to minimize grain boundary cracks,[34] mitigate surface-related failure mechanisms,[35] and enhance the structural stability of the cathode material, particularly at higher voltages.[36] Furthermore, the reduced specific surface area of single crystal particles mitigates side reactions between the electrolyte and electrode, improving electrochemical performance and prolonging cycling stability.[37] In this context, the combination of cathode doping, and surface manipulation has been proposed as a potential solution for addressing these issues.[22]

By systematically exploring the dual doping of Sb and Sn metal cathodes, we aim to refine the cathode composition to achieve a desired balance between energy density, cycling stability, and cost-effectiveness. This endeavor leverages the unique single-crystal morphology of cathode particles and the bulk doping of the cathode lattice to enhance performance synergistically.

Experimental section

Synthesis of cathode active materials

The cathode materials were synthesized by employing the sol–gel method. Citric acid (metal cations : citric acid = 1 : 1 in the molar ratio) was added to deionized water, mixed in a beaker, and heated at 50 °C on a hot plate. The solution was vigorously mixed at 500 rpm. A second solution containing a stoichiometric amount of nickel acetate tetrahydrate, manganese(II) acetate tetrahydrate, and lithium acetate dihydrate (5% excess) was dissolved in deionized water and prepared separately. This solution was added dropwise to the first one until completion. The pH was carefully maintained at 8.5–9.0 by adding ammonium hydroxide. Later, the solution was heated to 90 °C and kept there for about five hours until it reached a state of dryness. After mixing the resulting metal hydroxide with 1% antimony tin oxide by a planetary ball mill at 400 rpm for 1 h, the mixtures were calcinated at 500 °C for 5 h and 950 °C for 12 h in the air to obtain the corresponding lithiated metal oxide (Fig. 1). Subsequently, the resulting black powder was subjected to further ball milling, reheated at a heating rate of

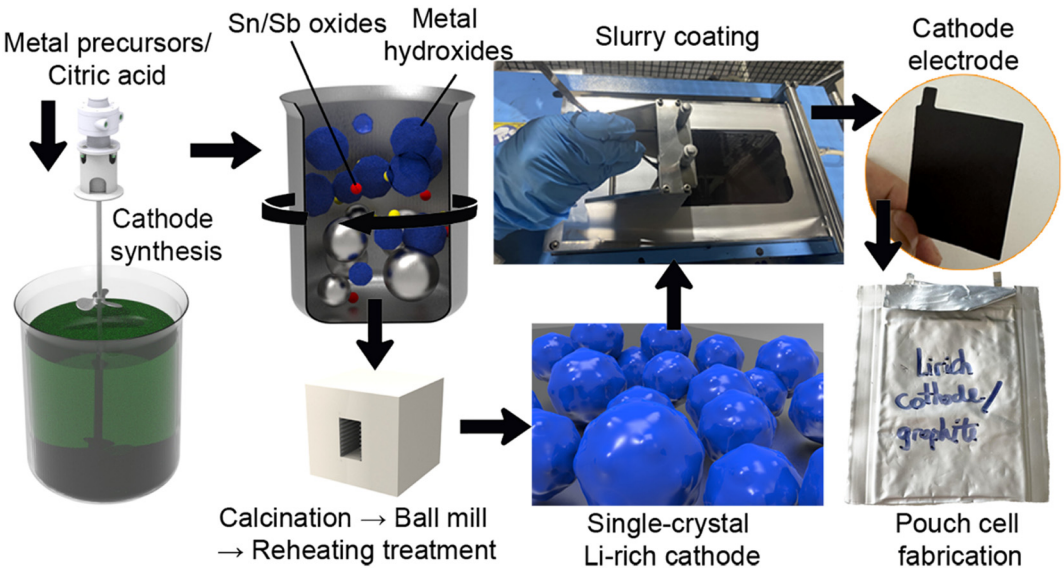

Fig. 1 Flow chart for the synthesis of Li-rich cobalt-free cathode and pouch cell preparation.

10 °C min^{-1} to 1050 °C, and held for 10 min to promote single-crystal formation. The doped Li-rich cathode is denoted as D-LR, and bare Li-rich cathode is denoted as B-LR.

Material characterization

Crystalline structures were analyzed using a Philips P.W. 1830 powder X-ray diffractometer with a Cu Kα-ray source, scanning within 10° to 90°. Microstructure and morphology were scrutinized using a JSM-6610LV SEM instrument and QUANTA FEG 250 scanning electron microscope equipped with energy-dispersive X-ray spectroscopy (EDS). Transmission electron microscopy (TEM) imaging was conducted utilizing an HF3300-environmental-CFE instrument equipped with a cold emission electron source to analyze detailed morphology and elemental distribution. The Field emission electron probe microanalyzer (FE-EPMA, JEOL JXA-8230) equipped with an energy dispersive spectrometer (EDS) was utilized to examine cross-section of the electrode. X-ray photoelectron spectroscopy (XPS) on a PerkinElmer Phi 5500 ESCA spectrophotometer probed the chemical and electronic states of the surface. High-resolution transmission electron microscopy (HRTEM) was performed using a Hitachi HF3300 Environmental-CFE-TEM operated at a voltage of 300 kV. HRTEM images were analyzed using the ImageJ software.

Slurry preparation

The cathode slurry was prepared by mixing the Li-rich cathode material, carbon black, and polyvinylidene fluoride binder in a specific weight ratio of 91 : 5 : 4 in *N*-methyl-2-pyrrolidone (NMP) solvent. The slurry was applied onto an aluminum foil, with the electrode thickness set at 60 μm. The anode slurry was prepared by mixing the commercial graphite, carbon black, carboxymethyl cellulose, and styrene–butadiene rubber (SBR) binder in a specific weight ratio of 94.5 : 1 : 2.25 : 2.25 in deionized water. Graphite slurry was coated on a copper foil, with the electrode thickness set at 50 μm.

Electrode preparation

The electrode preparation process included applying the wet slurry onto aluminum foil using a tape casting machine with a 10 cm long doctor blade at a low coating speed of 6 mm s^{-1}. The coated foil and separator were then dried overnight at 60 °C. Subsequently, the dried sheet underwent calendaring to increase tap density. Finally, the sheets were cut into electrodes measuring 56 mm in length and 43 mm in width using a semi-automatic slitting machine.

Pouch assembly

In an argon-filled glove box with H_2O and O_2 contents maintained below 1 ppm, the cathode electrode was stacked vertically (*Z*-stacked) with a graphite anode electrode measuring 54 mm in length and 41 mm in width. The anode and cathode were separated by a tri-layer separator consisting of polypropylene/polyethylene/polypropylene (PP/PE/PP) with a thickness of 25 μm (Celgard 2325). The electrolyte, which consisted of 1 M $LiPF_6$ dissolved in a mixture of ethylene carbonate (EC) and ethyl methyl carbonate (EMC) in a 3 : 7 volume ratio, was injected into the pouch cell at a volume of 5 ml per gram of cathode material. The sealed pouch cells were transferred to an oven at 50 °C for 12 hours to ensure thorough electrolyte distribution within the cell.

Electrochemical measurement

Galvanostatic charging/discharging profiles for the fabricated pouch cells were obtained on and 8-channel battery analyzer (MTI, USA) with a cut-off voltage range set at 2.0–4.8 V. Cyclic voltammetry (CV) plots and electrochemical impedance spectroscopy (EIS) were conducted on an Admiral Instruments Squidstat Plus potentiostat. Coin cells featuring Li metal as the counter electrode were employed for CV analyses. CV plots encompassed a potential range of 2–4.8 V, using a scan rate ranging from 0.2 to 1 mV s^{-1}. EIS curves were obtained under open circuit potential, in a frequency range of 2 MHz–0.1 Hz, with an excitation potential of 5 mV. The MEISP software was employed to estimate the experimental spectra to match the equivalent circuit.

Results and discussion

Morphology and structural analysis

As shown in Fig. 2, the SEM image of the Sb–Sn doped single-crystal particles exhibits very homogenous and smooth particles with well-defined interfaces and surfaces, along with a narrow diameter distribution ranging between 2 to 3 μm. The results of this analysis indicate that the use of re-heat treatment and dopants in the lattice, which serve as sintering agents and a crystal growth flux, are responsible for the higher crystallinity.[38] This assertion is supported by the higher intensity ratio of X-ray diffraction (XRD) reflections between (003) and (104), as depicted in Fig. 4.

High-resolution TEM images and elemental mapping (Fig. 2) clearly demonstrates the incorporation of Sb and Sn atoms within the cathode lattice at the atomic scale, rather than their mere surface deposition, indicating the successful incorporation of these dopants into the lattice structure. This observation underscores the homogeneous distribution of these elements within the studied particles, indicating consistent composition throughout the material.[38] This evidence of successful doping is pivotal, as integrating of Sb and Sn into the lattice can enhance structural stability and significantly improve the electrochemical performance of the cathode.[39] Complementary field-emission electron probe microanalysis (FE-EPMA) results and SEM/EDS imaging (Fig. S1 and S2†) further corroborate these findings by revealing a uniform distribution of Sb and Sn throughout the cross-section of the electrode.

The HRTEM imaging and corresponding FFT diffraction pattern display that the bare sample (Fig. 3) underwent a series of transformations upon cycling, notably manifesting numerous defects observable in its structure. This structural deformation likely originated from the dissolution of tran-

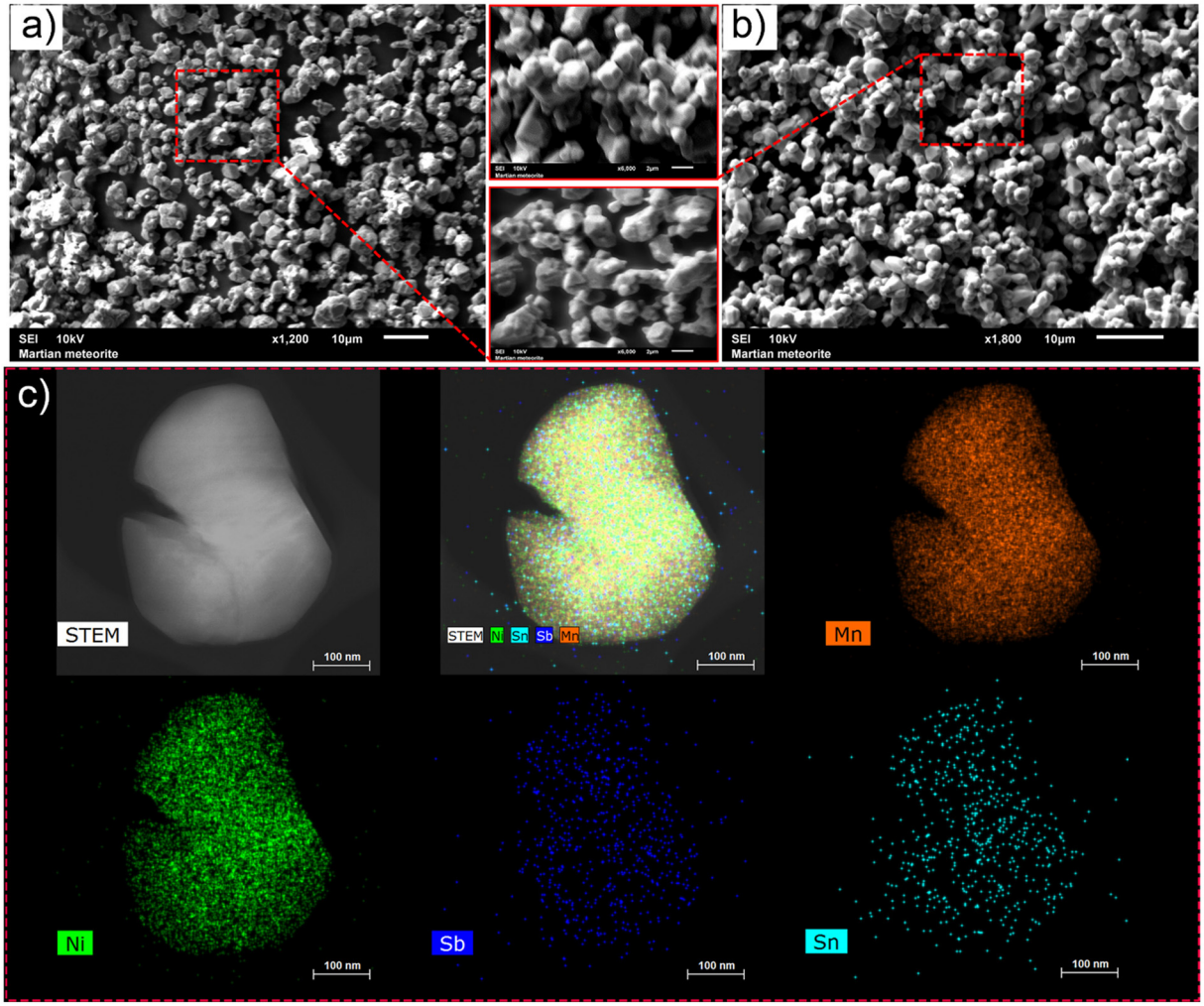

Fig. 2 SEM images of (a) B-LR and (b) D-LR and (c) high resolution transmission electron microscope (HRTEM) images and elemental maps of D-LR for Sn and Sb.

sition metal (TM) ions during the cycling process in high voltage, and the lattice structure changed from layer to deformed structure.[40] In contrast, the samples doped with Antimony (Sb) and Tin (Sn) (Fig. 3b) exhibited distinct characteristics. Even after undergoing the same number of cycling cycles at high voltage, these samples displayed surfaces characterized by a subtly altered appearance with well-maintained lattice fringes. As reported by Ahn *et al.*,[41] as the charging voltage increases, manganese ions (Mn^{4+}) within the transition metal (TM) layer exhibit a dynamic movement, transitioning between the octahedral site of the TM layer and the tetrahedral site of the lithium (Li) layer, contributing to the formation of a spinel phase. This spinel phase formation is a known contributor to damaging voltage decay in the battery. However, the introduction of appropriate cation doping into the lithium layer effectively blocks the migration path of manganese ions, minimizing structure evolution.[42] This strategy enhances the stability of the battery's structure, mitigating voltage decay and improving its overall performance and longevity.[43]

The resilience against structural degradation observed in co-doped samples suggests superior stability in the lattice structure compared to their undoped counterparts (Fig. 3c). Dual ion-doped cathodes predominantly exhibited a well-organized layered phase. This discrepancy suggests the presence of a stabilizing mechanism, likely attributable to the inclusion of trace amounts of dopants within the samples.[44] This enhancement typically leads to more effective preservation of structural integrity, resulting in improved cycling performance compared to the bare samples. These findings highlight the critical role of subtle adjustments in composition for tailoring material properties to meet specific functional and durability requirements across various applications.

The effect of (Sb, Sn) doping on the phase structure of lithium-rich material before and after battery cycling is inspected by XRD analysis, as shown in the Fig. 4. In contrast to the standard reference, the prominent characteristic peaks of Li-rich cathode materials correspond to a hexagonal layered structure with space group $R3m$.[45] Additionally, the well-

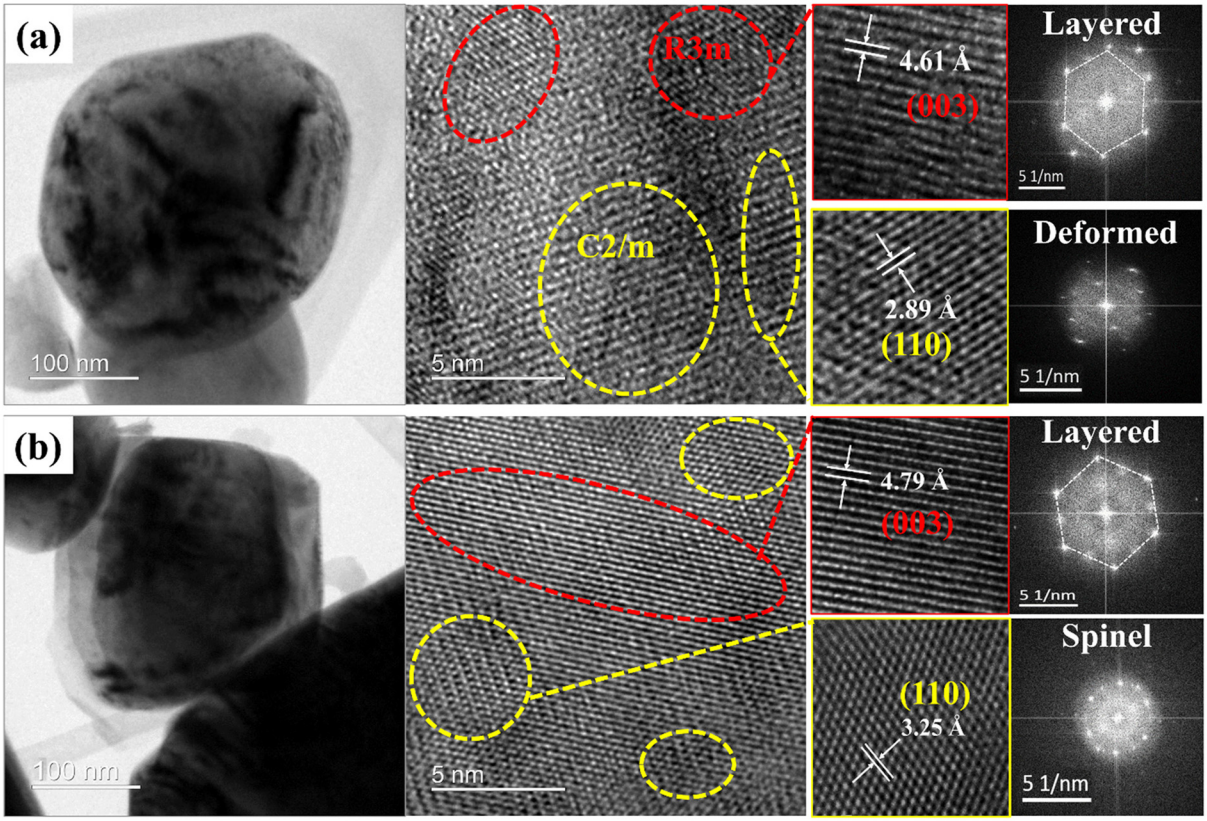

Fig. 3 HRTEM of the (a) B-LR and (b) D-LR.

defined structure is confirmed by the noticeable splitting between adjacent peaks (018)/(110). An additional weak superlattice peak, ranging from 20° to 23°, is found with space group $C2/m$ (monoclinic), attributed to Li_2MnO_3 containing $LiMn_6$ cations in the transition metal layers.[46] XRD examination shows a shift towards lower 2θ values in the (003) and (104) peaks of the Sb/Sn doped sample, indicating greater Li^+ ion diffusion.[47] This is supported by the extended graph of the (003) and (104) peaks in Fig. 4a. Moreover, the superlattice peak persists in the D-LR cathode compared to the pristine cathode even after undergoing 250 cycles of battery charge–discharge testing, as shown in Fig. 4b.

Rietveld refinement is conducted on the XRD data of all samples using high-score software to comprehensively investigate the effect of modifications on the material structure and explore the change in lattice parameters. The analysis showed that the B-LR sample's lattice parameters, a and c, are 2.8559 Å and 14.2461 Å, respectively. Subsequently, upon dual doping in the transition metal (TM) layer, these parameters increased to 2.8637 Å and 14.3890 Å, respectively. The thickness of the TM slab ($S(MO_2)$) and the lithium inter-slab ($I(LiO_2)$) in the layered structure are crucial parameters, elucidated by the strong interaction and lithium diffusion pathway. These parameters were calculated using two equations eqn (S1) and eqn (S2).† [48]

The analysis above indicates that Sn/Sb dual doping enlarges the inter-slab spacing, facilitating Li-ion diffusion by reducing the energy barrier of insertion/extraction. Meanwhile, the thickness of $S(MO_2)$ decreases with cooperative doping, favouring the stability of the layered structure, which is confirmed by calculated data as shown in Table 1. Additionally, the TM–O bond length increases, and the TM–O covalency decreases with the co-doping of Sn and Sb, further benefiting the stability of the layered structure. However, the c/a ratio of the samples before and after modification is greater than 4.9, indicating the layered structure of the material. Furthermore, the $I(003)/I(104)$ ratio of the modified samples is more significant than that of B-LR, indicating that the synthesized material has less Li/Ni mixing. Moreover, after cycling the battery up to 250 cycles, there is no change in $I(003)/I(104)$, indicating no mixing of Li/Ni compared to B-LR.

Thus, it is concluded that Sn/Sb co-doping enhances the battery's performance by increasing the Li^+ diffusion rate, stabilizing the layered structure, and subsequently enhancing the high-rate capability.

The impact of the Sb and Sn elements on the chemical valence and reactivity in the cathode material is examined using XPS spectra. Fig. 5 depicts the Mn, Ni, Sn, and Sb electronic states before and after the doping. The peaks 641.5 eV and 653 eV correspond to Mn $2p_{3/2}$ and Mn $2p_{1/2}$. Both peaks consist of two smaller peaks, Mn^{3+} and Mn^{4+} ions. It was found that there was some reduction of Mn^{4+} and Mn^{3+} peaks after the doping. Supporting the TEM findings, the Mn atoms

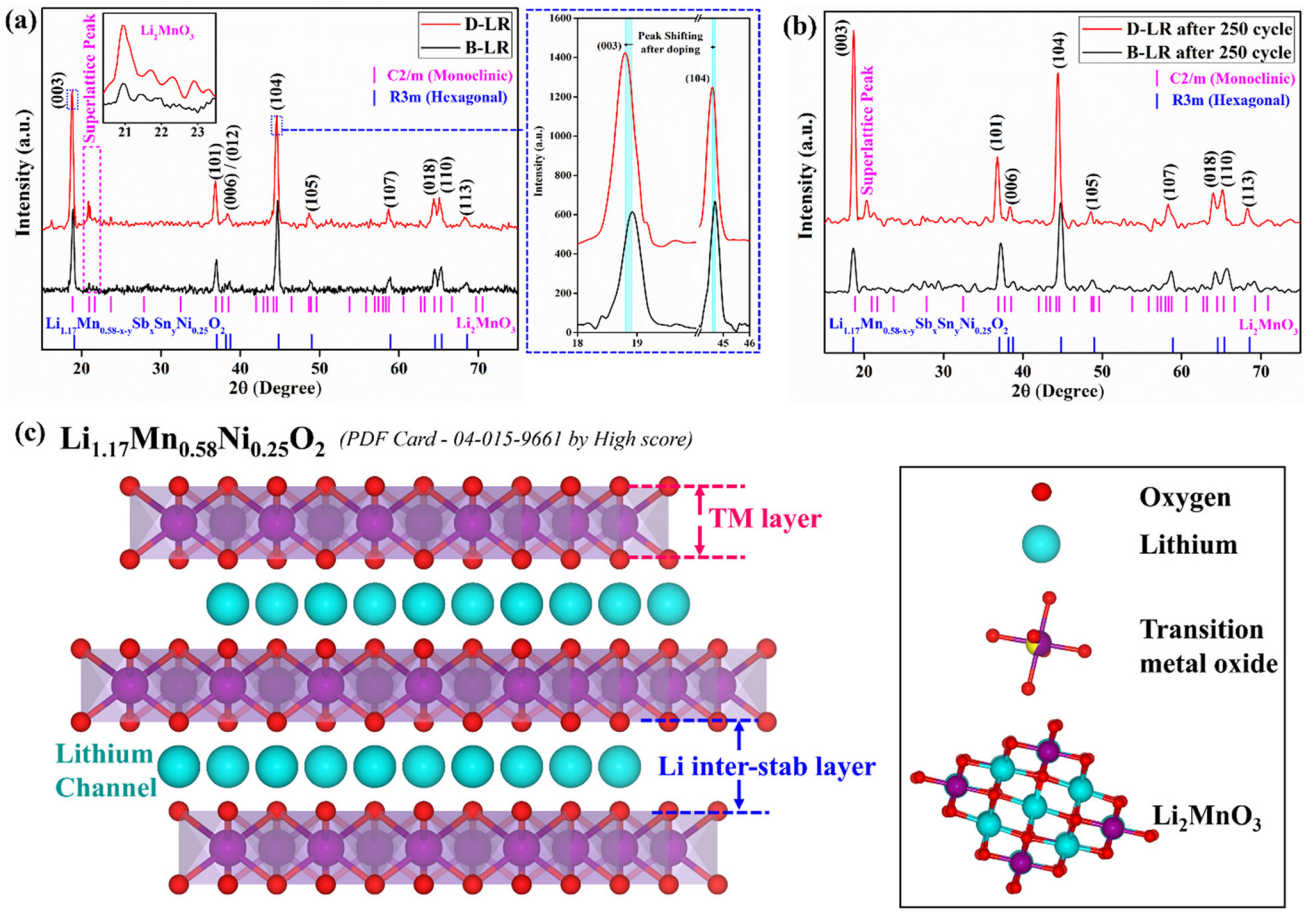

Fig. 4 XRD patterns of D-LR and B-LR.

Table 1 Rietveld refinement results of $Li_{1.17}Mn_{0.58-x-y}Sn_xSb_yNi_{0.25}O_2$ based *R*3*m* structure

Samples	*a*/*b* (Å)	*c* (Å)	*c*/*a*	Z_{ox}	$S(MO_2)$	$I(LiO_2)$	$I_{(003)}/I_{(104)}$
B-LR	2.8559	14.2460	4.9883	0.2424	2.5909	2.1578	0.9207
D-LR	2.8637	14.3890	5.0250	0.2630	2.0241	2.7723	1.2186
B-LR 250	2.8797	14.2273	4.9405	0.2417	2.6074	2.1350	0.4792
D-LR 250	2.8951	14.3057	4.9413	0.2579	2.1583	2.6103	1.2167

cause an increase in the crystal lattice gap, thereby increasing the amount of space available to store ions.[49,50] As for the Ni, the binding energies of Ni 2p3/2 and Ni 2p1/3 peaks are 859.2 eV and 872.5 eV, respectively. The split peak of nickel ions is associated with the satellite peak at 861 eV.[51] Furthermore, the binding energies of Ni^{2+} and Ni^{3+} correspond to 854.3 eV and 855.2 eV. It was noted that Sb influences the valence of the Ni^{2+} and Ni^{3+} ions, and the area of the dopped peaks is increasing by 12% and 26%, with slight shift to 855.0 eV and 856.1 eV for Ni^{2+} and Ni^{3+} ions respectively.[52,53] This can be explained by the fact that the electronegativity of the doping element is greater than that of the original element, resulting in a decrease in the electron density around the unit and an increase in the binding energy.[54] Peaks Sn 3d3/2 and Sn 3d5/2 consist of coexisting Sn^{2+} and Sn^{4+}, which can be seen in Fig. 5. Sn^{2+} state assigned to 487.1 and 495.2 eV and Sn^{4+} to 488.1 and 496.2 eV.[55] By integrating the area under each composition curve, the Sn^{2+} to Sn^{4+} ratio was determined to be 0.81. The inclusion of Sn in the composition facilitates the morphology of the ligaments. It modifies the internal space of the system through the use of Sn nanocrystals to retain their dimensions after lithiation.[56] The oxygen metal (O–M) content of the cathode material represented by the O 1s peak at 529.6 eV increased for the dopped sample (Fig. 5).[42]

Electrochemical characterizations

Fig. 6 exhibits the initial charge–discharge curves of the D-LR and B-LR in the 2.0–4.8 V range at room temperature at 1C rate. The discharge capacities at 250 cycles for Sn/Sb doped Li-rich and bare Li-rich are 156.74 mA h g^{-1} and 127.44 mA h

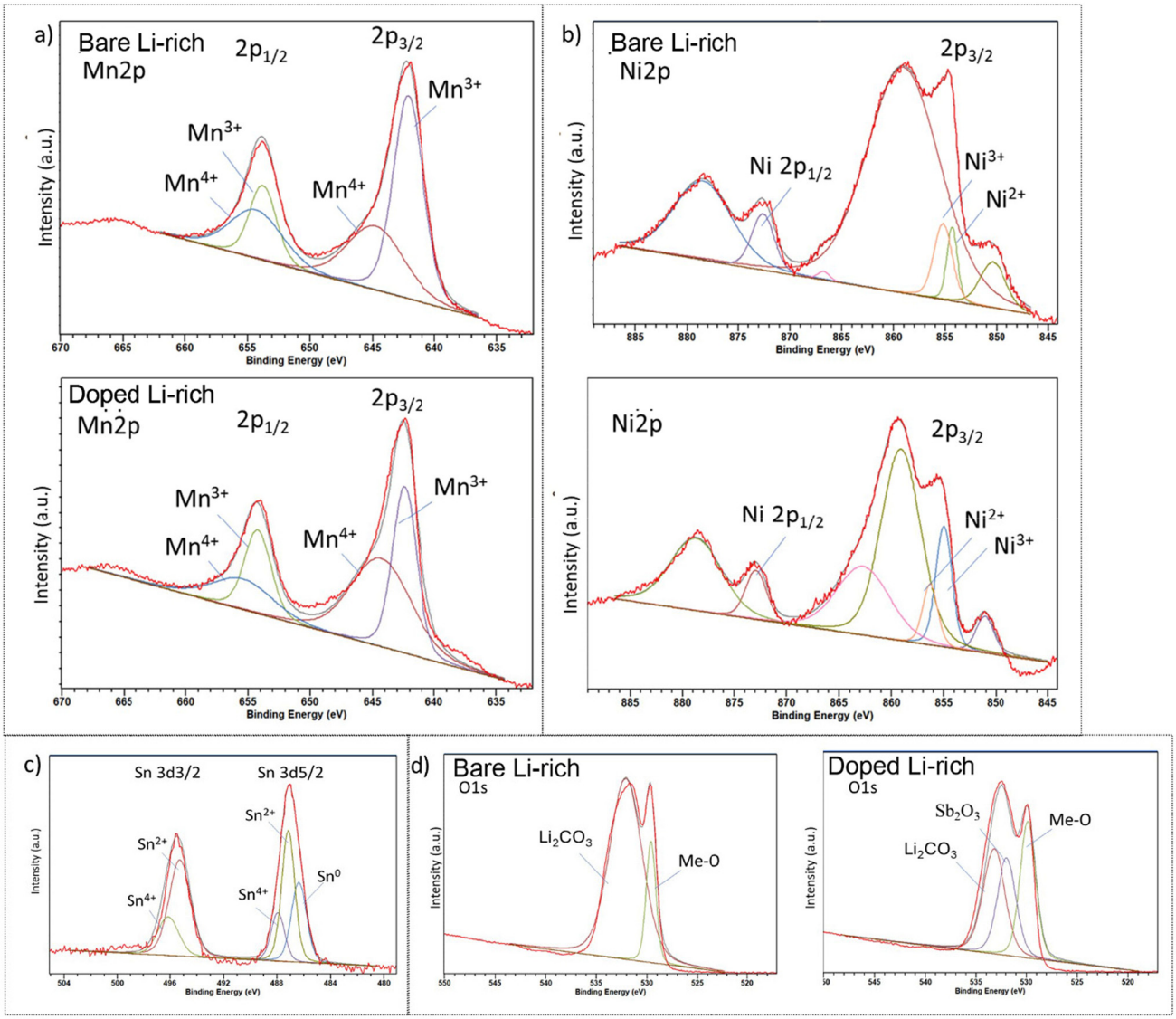

Fig. 5 XPS spectra of the (a) Mn 2p, (b) Ni 2p, (c) Sn 3d and (d) O 1s in B-LR and D-LR.

g^{-1}, respectively, corresponding to percentage capacity retention of 82.05 and 72.16. This means the doped LR has better cation and anionic redox reversibility.[57] Numerous studies have reported a significantly lower specific capacity at a 1C rate compared to our findings.[58,59] Due to the trace amount of Sn and Sb doping, the persistent escalation of polarization throughout cycling is effectively mitigated, thereby enhancing the cyclability of the doped Li-rich cathode over extended cycling periods. Some studies have investigated surface coating and found inferior results compared to bulk doping.[60] This suggests that bulk doping plays a critical role in stabilizing the structure, providing more stability and reducing undesirable reactions.[61] Zang *et al.*[31] suggest that the enhanced cycling performance of the doped material may result from the even dispersion of dopant elements, acting as pinning sites to impede the transition from layered to spinel structures. In addition, the superior cycling stability of the doped sample can be attributed to the increase in lattice parameter values of *c* (Table 1), which in turn enlarges the transport pathway for Li^+ ions and facilitates intercalation/deintercalation processes of Li^+.[62] Moreover, there is a notable correlation between the absence of doping metals within the cathode lattice and decline in irreversible capacity following the initial cycle. This observation is based on the initially low coulombic efficiency observed for B-LR (53%). The issue arises from the irreversible migration of transition metals, which obstruct the diffusion pathways of Li-ion,[63] thereby causing the problem. As shown in Fig. 5a and b, the D-LR samples exhibited electrochemical behavior in the second charge cycle, characterized by a long plateau around 4.5 V, which is associated with the oxidation of O^{2-} to $O^{(2-n)}$.[64,65] In contrast, the B-LR samples displayed a more subtle plateau, indicating that the evolution mechanism

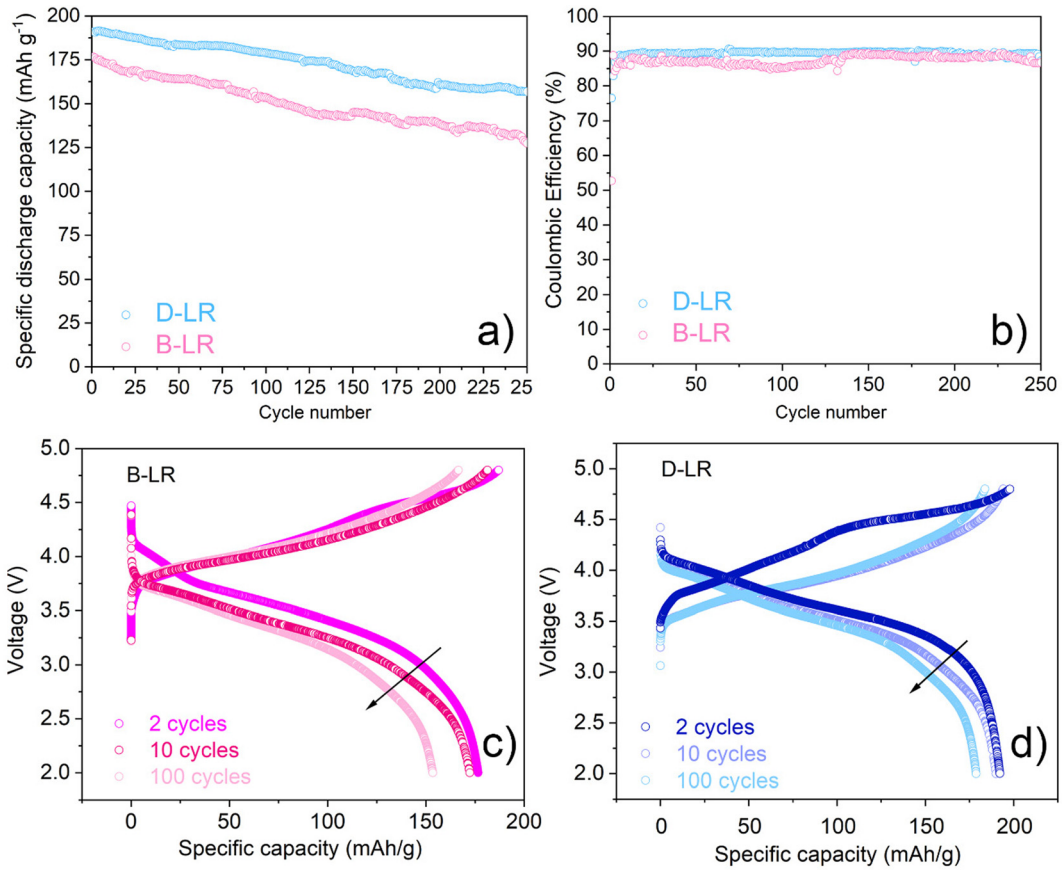

Fig. 6 (a) The cycling performance and (b) coulombic efficiency of B-LR and D-LR, and charge/discharge profiles of (c) B-LR and (d) D-LR full cells (1C-rate).

of phase transformation has already occurred. Despite the absence of a distinct plateau after 10 cycles, some degree of anionic redox reactions may still occur beyond 4.5 V for both B-LR and D-LR, although to a lesser extent. The discharge platform of doped materials surpasses bare Li-rich counterparts, indicating that including that the addition of Sn and Sb dopants effectively mitigates phase transformation and electrode polarization. The superior capacity performance of doped electrodes can be attributed to reduced Li/Ni disordering and the creation of expanded pathways for Li-ion insertion and extraction, as evidenced by XRD analysis (Table 1). These findings illustrate the effectiveness of bulk Sn and Sb doping in enhancing the cycling stability of Li-rich cathodes. Lower charge voltage and higher discharge voltage imply reduced electrochemical polarization for D-LR, indicating enhanced Li-ion diffusion kinetics.[57] Research on cobalt-free cathodes has revealed considerable capacity fading and marked potential hysteresis between charge and discharge reactions.[66,67] The arrow in Fig. 6c and d highlights a significant voltage fading observed for B-LR, possibly indicating a phase transformation within the cathode lattice.

It is recognized that the shape of peaks and their current responses to sweep rates indicate the kinetics of Li^+ extraction and reinsertion at the interface of the electrode/electrolyte and the rate of Li^+ diffusion within the lithium battery.[68] Fig. 7a and b illustrates the cyclic voltammograms (CVs) of B-LR and D-LR obtained at various scan rates ranging from 1 mV s^{-1} to 0.2 mV s^{-1}, within the voltage span of 2.0–4.8 V. With increasing scan rates, both oxidation and reduction peaks shift towards higher and lower potentials, respectively. As can be seen, the D-LR sample exhibits more symmetric and slightly sharper peaks than the B-LR sample. Additionally, both electrodes exhibit two anodic peaks around 4.1 V and 4.6 V, as depicted in Fig. 6a and b. The peak at approximately 4.8 V, attributed to the elimination of lithium and oxygen from the Li_2MnO_3 phase, disappears after the first scan run.[69] Furthermore, it is evident that the peak at 4.6 V during the initial cycle notably diminishes after doping, indicating that Sn and Sb doping could mitigate oxygen release during the initial charging process. In the initial discharge phase, the CV curve displays a broad hump within the voltage range of 3.4–4.2 V, corresponding to the reduction of Ni^{4+} and Mn^{4+}. The relatively significant potential difference (ΔV) between oxidation and reduction peaks is depicted in Fig. 7a and b. The voltage difference (ΔE) between the anodic and cathodic peaks illustrates electrochemical reversibility.[70] The ΔE values for D-LR and B-LR electrodes are 0.54 V and 0.82 V, respectively, suggesting that the doping strategy promotes decreased polar-

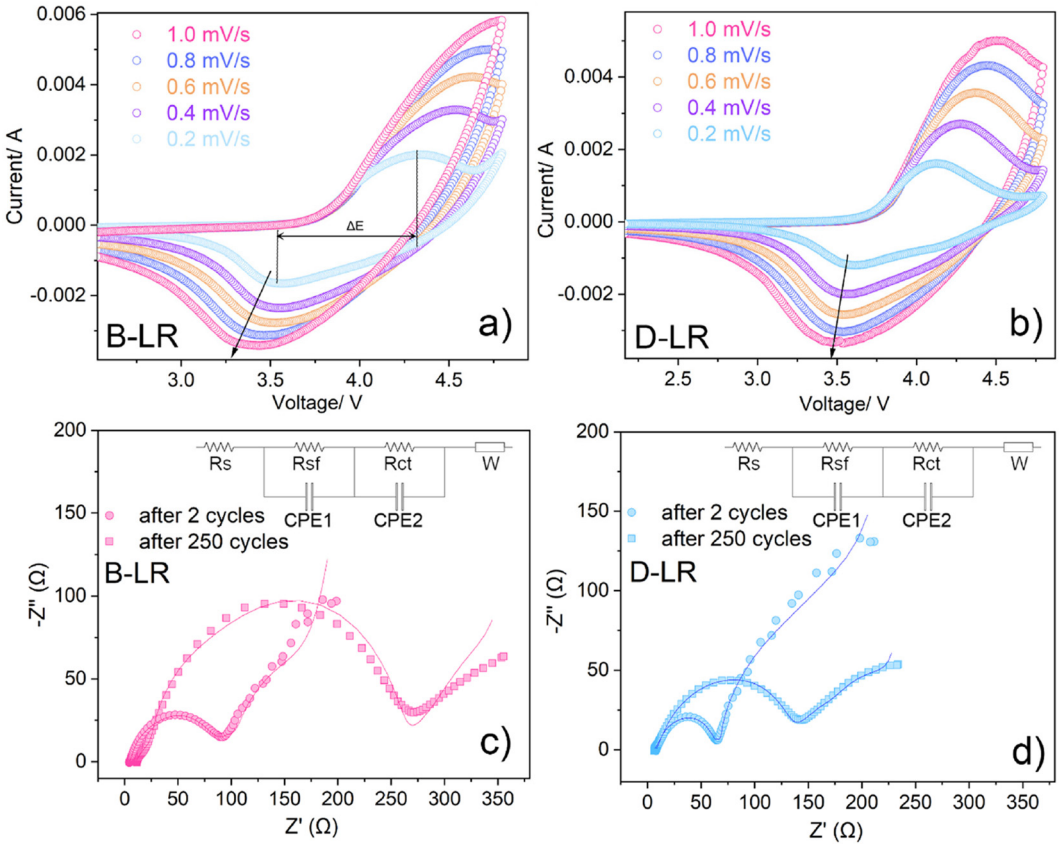

Fig. 7 EIS of B-LR and D-LR before cycle and after 250 cycles.

ization and enhanced reversibility of the Li-rich cathode. These CV results validate the favorable cycling stability of the D-LR cathode.[9] The diffusion coefficient of Li^+ ion can be determined using the Randles–Sevcik equation (eqn (S3)†).[71] The Li^+ ion diffusivity values of B-LR and D-LR were determined as 2.10×10^{-9} cm^2 s^{-1} and 6.83×10^{-9} cm^2 s^{-1}, respectively, potentially due to increased diffusion activity during Li^+ de/intercalation.[49]

To explore the enhancement of electrochemical properties and reaction kinetics through Sb and Sn doping, electrochemical impedance spectroscopy (EIS) analyses were undertaken. Nyquist impedance curves and the fitting curves with the equivalent circuit are shown in Fig. 7c and d. Each Nyquist profile typically consists of a pair of semicircles or a single semicircle with overlapping arcs.[72] Within this representation, the semicircle corresponding to higher frequencies usually represents the resistance of the solid–electrolyte interface (SEI) film and interface (R_{sf}). In contrast, the intermediate semicircle indicates the charge transfer resistance (R_{ct}).[73] In addition, the ohmic resistance (R_s) of the electrolyte can be acquired from the high-frequency intercept with the Z'-axis of the Nyquist plot, and the low-frequency linear slope represents the ion diffusion resistance (W_o) in the cathode.[74] The utilization of a two-electrode cell for measurements raises the possibility that the impedance detected may originate partially from the Li anode. Nonetheless, it is reasonable to assume that the predominant contribution of the impedance arises from the cathode.[32] The R_s, R_{sf} and R_{ct} values are calculated according to the equivalent circuit diagram (Fig. 7c and d) and shown in Table 2. For the fresh electrodes, impedance resistance for L-RH was slightly higher than D-LH. Although, the variance in the ohmic resistance (R_s) between both samples is minimal. Nevertheless, the decreased R_{st} value observed in D-LR can be attributed to the suppression of side reactions with the electrolyte, thereby reducing the formation of a thick SEI layer.[75] In addition, it was observed that the charge transfer resistance (R_{ct}) of the B-LR electrode increased notably after 250 cycles, in contrast to the D-LR electrode, where the increase surpassed twice its initial value. This suggests that the doping strategy of Sn and Sb in LR effectively reduced structural transformation.[76] These results further support the positive impact of

Table 2 Data from the EIS fitting curve

	Number of cycles	R_{es}	R_{sf}	R_{ct}
Bare Li-rich	2	5.38	11.10	63.42
	250	12.49	14.63	217.56
Doped Li-rich	2	8.73	6.04	40.98
	250	7.99	13.16	107.88

including Sn and Sb metals in preventing the manganese dissolution[77] and subsequent irreversible phase changes, thus leading to better cyclability.[78] These findings support the perception of the beneficial effects of incorporating Sn and Sb metals in mitigating metal dissolution[77] and subsequent irreversible phase alterations.[78] The even distribution of these metals throughout the cathode framework is beneficial for reducing stress caused by structural changes and preventing the pulverization of cathode particles.[79]

Conclusion

In conclusion, we have demonstrated a facile and efficient approach for incorporating Sn and Sb into the cathode bulk phase while concurrently stabilizing its mechanical and electronic properties. Utilizing a sol–gel method followed by reheat treatment, we engineered Li-rich layered cathodes with a unique single-crystal structure. The cooperative combination of morphology manipulation and dual ion doping significantly mitigated cation mixing and enlarged Li interstitial sites within the cathode lattice. This synergistic doping effect was instrumental in enhancing the performance of the electrodes. A comparative investigation between the dually doped (D-LR) and undoped (B-LR) electrodes demonstrated that D-LR yielded superior discharge and reversible capacities, especially under a 1C charge–discharge rate. The enhanced cycling performance and discharge capacity of D-LR can be attributed to reduced electrochemical polarization, improved Li-ion diffusion, higher electrochemical activity, and superior kinetic behavior. Notably, the doped LR sample showcased a remarkable capacity performance of 191.01 mA h g^{-1} with capacity retention exceeding 87.24% after 250 cycles at 1C, surpassing bare LR. Consequently, the exceptional cycling stability, high capacity, and structure stability designate Sn/Sb dual-doped Li-rich cathodes as promising candidates for positive electrode materials, offering commendable electrochemical performance.

Author contributions

O. A. T. D. and F. A.: conceptualization, formal analysis, investigation, methodology, software, validation, writing – original draft, review & editing; K. R.: data curation, software, validation, writing – original draft, review & editing; V. P.: data curation, software, validation, writing – original draft, review & editing; V. K. T.: formal analysis, investigation, methodology; M. S.: conceptualization, funding acquisition, project administration, resources, supervision.

Data availability

The authors confirm that the data supporting the findings of this study are available within the article and its ESI.† Raw data that support the findings of this study are available from the corresponding authors upon reasonable request.

Conflicts of interest

There are no conflicts to declare.

Acknowledgements

The authors express their gratitude to MITACS (Canada) and Zentek Ltd for their financial support and to Ford Motor Company of Canada for its in-kind contribution to this project.

References

1 M. M. Rampai, C. B. Mtshali, N. S. Seroka and L. Khotseng, *RSC Adv.*, 2024, **14**, 6699–6718.
2 K. Davis and G. P. Demopoulos, *RSC Sustainability*, 2023, **1**, 1932–1951.
3 M. M. Khan, A. K. Kadian, R. P. Sharma, S. M. Hasnain, A. Mohamed, A. E. Ragab, A. Zare and S. Pandey, *Sustainability*, 2023, **15**, 9084.
4 H. R. Oliveira Filho, H. Zanin, R. S. Monteiro, M. H. P. Barbosa and R. F. Teófilo, *J. Energy Storage*, 2024, **82**, 110536.
5 V. K. Tomer, R. L. Kumawat, O. A. Titton Dias, R. Malik, G. C. Schatz and M. Sain, *J. Mater. Chem. A*, 2024, **12**, 15814–15828.
6 J. Jeevanandam, S. F. Kiew, S. Boakye-Ansah, S. Y. Lau, A. Barhoum, M. K. Danquah and J. Rodrigues, *Nanoscale*, 2022, **14**, 2534–2571.
7 R. Schmuch, R. Wagner, G. Hörpel, T. Placke and M. Winter, *Nat. Energy*, 2018, **3**, 267–278.
8 P. Alves Dias, D. Blagoeva, C. Pavel and N. Arvanitidis, *Cobalt: demand-supply balances in the transition to electric mobility*, Publications Office of the European Union, Luxembourg, Luxembourg, 2018.
9 T.-F. Yi, Y.-M. Li, X.-D. Cai, S.-Y. Yang and Y.-R. Zhu, *Mater. Today Energy*, 2017, **4**, 25–33.
10 J. Guo, Y. Xu, M. Exner, X. Huang, Y. Li, Y. Liu, H. Wang, J. Kowal, Q. Zhang, P. K. Kristensen, D. Wang, K. Pedersen, L. Gurevich, D.-I. Stroe and P. Adelhelm, *Adv. Energy Mater.*, 2024, 2400190.
11 S. Kang, X. Wei, Y. Chu, Y. Mu, L. Zou, X. Xu, Q. Zhang and L. Zeng, *J. Mater. Chem. A*, 2024, **12**, 9584–9593.
12 C. Liu, S. Zhang, Y. Feng, X. Miao, G. Yang and J. Li, *Nanoscale*, 2022, **14**, 65–75.
13 Q. Zhao, M. Zhang, Z. Ye, Y. Li, L. Qiu, Z. Zheng, Y. Liu, B. Zhong, Y. Song and X. Guo, *Nanoscale*, 2023, **15**, 3326–3336.
14 H.-H. Ryu, H. H. Sun, S.-T. Myung, C. S. Yoon and Y.-K. Sun, *Energy Environ. Sci.*, 2021, **14**, 844–852.

15 S. Kang, D. Choi, H. Lee, B. Choi and Y.-M. Kang, *Adv. Mater.*, 2023, **35**, 2211965.
16 W. Zhu, J. Zhao, M. Yang, J. Zhan, H. Su, C. Zeng, Z. Li, J. Zhang, Y. Chen and Y. Xu, *J. Mater. Chem. A*, 2024, **12**, 15194–15202.
17 H. Zhuo, A. Zhang, X. Huang, J. Wang and W. Zhuang, *Inorg. Chem. Front.*, 2021, **8**, 4590–4609.
18 S. K. Martha, J. Nanda, G. M. Veith and N. J. Dudney, *J. Power Sources*, 2012, **199**, 220–226.
19 W. He, Q.-S. Xie, J. Lin, B.-H. Qu, L.-S. Wang and D.-L. Peng, *Rare Met.*, 2022, **41**, 1456–1476.
20 I. Bloom, L. Trahey, A. Abouimrane, I. Belharouak, X. Zhang, Q. Wu, W. Lu, D. P. Abraham, M. Bettge, J. W. Elam, X. Meng, A. K. Burrell, C. Ban, R. Tenent, J. Nanda and N. Dudney, *J. Power Sources*, 2014, **249**, 509–514.
21 D. A. Santos, S. Rezaei, D. Zhang, Y. Luo, B. Lin, A. R. Balakrishna, B.-X. Xu and S. Banerjee, *Chem. Sci.*, 2023, **14**, 458–484.
22 Z.-X. Huang, X.-L. Zhang, X.-X. Zhao, H.-Y. Lü, X.-Y. Zhang, Y.-L. Heng, H. Geng and X.-L. Wu, *J. Mater. Sci. Technol.*, 2023, **160**, 9–17.
23 B. Wang, J. Cui, Z. Li, H. Wang, D. Zhang, Q. Wang, H. Sun and Y. A. Wu, *Mater. Chem. Front.*, 2023, **7**, 2570–2594.
24 M. Zhou, J. Zhao, X. Wang, J. Shen, W. Tang, Y. Deng and R. Liu, *Chin. Chem. Lett.*, 2023, **34**, 107793.
25 Z.-X. Huang, Z.-Y. Gu, Y.-L. Heng, E. Huixiang Ang, H.-B. Geng and X.-L. Wu, *Chem. Eng. J.*, 2023, **452**, 139438.
26 M. Chen, E. Zhao, D. Chen, M. Wu, S. Han, Q. Huang, L. Yang, X. Xiao and Z. Hu, *Inorg. Chem.*, 2017, **56**, 8355–8362.
27 H. Kondo, Y. Takeuchi, T. Sasaki, S. Kawauchi, Y. Itou, O. Hiruta, C. Okuda, M. Yonemura, T. Kamiyama and Y. Ukyo, *J. Power Sources*, 2007, **174**, 1131–1136.
28 C.-C. Wang, Y.-C. Lin and P.-H. Chou, *RSC Adv.*, 2015, **5**, 68919–68928.
29 H. Sun, Z. Cao, T. Wang, R. Lin, Y. Li, X. Liu, L. Zhang, F. Lin, Y. Huang and W. Luo, *Mater. Today Energy*, 2019, **13**, 145–151.
30 Z. Ma, J. Huang, J. Quan, L. Mei, J. Guo and D. Li, *RSC Adv.*, 2016, **6**, 20522–20531.
31 Y. Zang, X. Sun, Z.-F. Tang, H.-F. Xiang and C.-H. Chen, *RSC Adv.*, 2016, **6**, 30194–30198.
32 X. Li, H. Xin, Y. Liu, D. Li, X. Yuan and X. Qin, *RSC Adv.*, 2015, **5**, 45351–45358.
33 S. Lu, L. Tang, H. Wei, Y. Huang, C. Yan, Z. He, Y. Li, J. Mao, K. Dai and J. Zheng, *Electrochem. Energy Rev.*, 2022, **5**, 15.
34 J. Li, H. Hu, J. Wang and Y. Xiao, *Carbon Neutralization*, 2022, **1**, 96–116.
35 L.-T. Li, Y.-F. Chen, Y.-C. Liu, Q. Zhang, J.-W. Wu and Q.-H. Yuan, *Rare Met.*, 2023, **42**, 830–837.
36 P. Yan, J. Zheng, M. Gu, J. Xiao, J.-G. Zhang and C.-M. Wang, *Nat. Commun.*, 2017, **8**, 14101.
37 Z.-X. Huang, X.-L. Zhang, X.-X. Zhao, Y.-L. Heng, T. Wang, H. Geng and X.-L. Wu, *Sci. China Mater.*, 2023, **66**, 79–87.
38 L. Zhou, J. Liu, L. Huang, N. Jiang, Q. Zheng and D. Lin, *J. Solid State Electrochem.*, 2017, **21**, 3467–3477.
39 R. Yang, L. Chang, S. Luo, X. Bi, W. Yang, K. Cai, A. Wei and Z. Hou, *J. Mater. Chem. C*, 2024, **12**, 4961–4976.
40 M. Zhou, J. Zhao, X. Wang, J. Shen, J.-L. Yang, W. Tang, Y. Deng, S.-X. Zhao and R. Liu, *RSC Adv.*, 2022, **12**, 32825–32833.
41 J. Ahn, R. Giovine, V. C. Wu, K. P. Koirala, C. Wang, R. J. Clément and G. Chen, *Adv. Energy Mater.*, 2023, **13**, 2300221.
42 S. Park, S. Y. Jeong, T. K. Lee, M. W. Park, H. Y. Lim, J. Sung, J. Cho, S. K. Kwak, S. Y. Hong and N.-S. Choi, *Nat. Commun.*, 2021, **12**, 838.
43 L. Luo, Y. Zhen, Y. Lu, K. Zhou, J. Huang, Z. Huang, S. Mathur and Z. Hong, *Nanoscale*, 2020, **12**, 230–238.
44 B. Li, X. Wang, Y. Gao, B. Wang, J. Qiu, X. Cheng and D. Dai, *J. Materiomics*, 2019, **5**, 149–155.
45 Y. Tang, Z. Chen, F. Lin, H. Zhu, J. Wen, Y. Wang, M. Bai and J. Duan, *J. Alloys Compd.*, 2023, **959**, 170552.
46 Y. Li, C. Wu, Y. Bai, L. Liu, H. Wang, F. Wu, N. Zhang and Y. Zou, *ACS Appl. Mater. Interfaces*, 2016, **8**, 18832–18840.
47 Y. Liu, D. Ning, L. Zheng, Q. Zhang, L. Gu, R. Gao, J. Zhang, A. Franz, G. Schumacher and X. Liu, *J. Power Sources*, 2018, **375**, 1–10.
48 J. Bains, L. Croguennec, J. Bréger, F. Castaing, S. Levasseur, C. Delmas and Ph. Biensan, *J. Power Sources*, 2011, **196**, 8625–8631.
49 T. Liang, W. Zeng, L. Yang, S. Liu, Y. Huang, H. He, X. Chen and A. He, *J. Alloys Compd.*, 2022, **910**, 164862.
50 K. Chen, M. Wang, G. Li, Q. He, J. Liu and F. Li, *Materials*, 2018, **11**, 601.
51 A. J. Naylor, E. Makkos, J. Maibach, N. Guerrini, A. Sobkowiak, E. Björklund, J. G. Lozano, A. S. Menon, R. Younesi, M. R. Roberts, K. Edström, M. S. Islam and P. G. Bruce, *J. Mater. Chem. A*, 2019, **7**, 25355–25368.
52 Z.-Y. Wu, L. Deng, J.-T. Li, S. Zanna, A. Seyeux, L. Huang, S.-G. Sun, P. Marcus and J. Światowska, *Batteries*, 2022, **8**, 271.
53 A. de O. Jorgetto, M. V. Boldrin Zanoni and M. O. Orlandi, *Sci. Rep.*, 2023, **13**, 14774.
54 B. Philippe, R. Dedryvère, J. Allouche, F. Lindgren, M. Gorgoi, H. Rensmo, D. Gonbeau and K. Edström, *Chem. Mater.*, 2012, **24**, 1107–1115.
55 P. Weng, Q. Cai, L. Zhang, H. Wu, K. Wu and J. Guo, *Solid State Sci.*, 2022, **131**, 106960.
56 H. Ying and W.-Q. Han, *Adv. Sci.*, 2017, **4**, 1700298.
57 W. Su, H. Song, H. Mao, D. Wang, Y. Liu, D. Xiao, Y. Lyu and B. Guo, *Chem. Eng. J.*, 2023, **475**, 146350.
58 A. M. Pillai, P. S. Salini, B. John, V. S. Nair, K. Jalaja, S. SarojiniAmma and M. T. Devassy, *Ionics*, 2022, **28**, 5005–5014.
59 K. Redel, A. Kulka, K. Walczak, A. Plewa, E. Hanc, M. Marzec, L. Lu and J. Molenda, *Chem. Eng. J.*, 2021, **424**, 130293.
60 H. Qian, H. Ren, Y. Zhang, X. He, W. Li, J. Wang, J. Hu, H. Yang, H. M. K. Sari, Y. Chen and X. Li, *Electrochem. Energy Rev.*, 2022, **5**, 2.

61 P. Oh, S.-M. Oh, W. Li, S. Myeong, J. Cho and A. Manthiram, *Adv. Sci.*, 2016, **3**, 1600184.
62 H. Li, H. Guo, Z. Wang, J. Wang, X. Li, N. Chen and W. Gui, *Int. J. Hydrogen Energy*, 2018, **43**, 11109–11119.
63 K. Redel, A. Kulka, K. Walczak, A. Plewa, E. Hanc, M. Marzec, L. Lu and J. Molenda, *Chem. Eng. J.*, 2021, **424**, 130293.
64 Y. Pei, Q. Chen, M. Wang, B. Li, P. Wang, G. Henkelman, L. Zhen, G. Cao and C.-Y. Xu, *Nano Energy*, 2020, **71**, 104644.
65 H. Wu, J. Dong, Y. Zhang, L. Lin, G. Gao, T. Li, X. Yi, B. Sa, J. Wang, L. Wang, J. Li, K. Amine, D.-L. Peng and Q. Xie, *Adv. Funct. Mater.*, 2023, **33**, 2303707.
66 A. Abdel-Ghany, A. M. Hashem, A. Mauger and C. M. Julien, *Energies*, 2020, **13**, 3487.
67 W. Ke, Y. Jiang, Y. Han, L. Deng, Y. Xia, L. Que, F. Yu, Y. Wang and Z. Wang, *Ionics*, 2021, **27**, 3837–3846.
68 P. Gao, G. Yang, H. Liu, L. Wang and H. Zhou, *Solid State Ionics*, 2012, **207**, 50–56.
69 P. Vanaphuti, J. Chen, J. Cao, K. Bigham, B. Chen, L. Yang, H. Chen and Y. Wang, *ACS Appl. Mater. Interfaces*, 2019, **11**, 37842–37849.
70 L. Wu, X. Tang, Z. Rong, X. Chen, J. Huang, T. Chen, X. Fang, Y. Wang and W. Dang, *Appl. Surf. Sci.*, 2019, **484**, 21–32.
71 S.-B. Kim, H. Kim, D.-H. Park, J.-H. Kim, J.-H. Shin, J.-S. Jang, S.-H. Moon, J.-H. Choi and K.-W. Park, *J. Power Sources*, 2021, **506**, 230219.
72 L. Wang, M. Geng, X. Ding, C. Fang, Y. Zhang, S. Shi, Y. Zheng, K. Yang, C. Zhan and X. Wang, *Int. J. Miner., Metall. Mater.*, 2021, **28**, 538–552.
73 X. Guo, Q. Zhou, C. Wang, Y. Cao, X. Yang, S. Wei, W. Xu, S. Chen, K. Zhu, P. Zhang, H. Shou, Y. Wang, P. J. Chimtali, X. Wu, L. Song and X. Liu, *Small*, 2024, 2400099.
74 M. Zhao, Y. Lu, Y. Yang, M. Zhang, Z. Yue, N. Zhang, T. Peng, X. Liu and Y. Luo, *Nanoscale*, 2021, **13**, 13085–13094.
75 W. Liu, P. Oh, X. Liu, S. Myeong, W. Cho and J. Cho, *Adv. Energy Mater.*, 2015, **5**, 1500274.
76 Z. Wang, Y. Yin, G. He, H. Zhao and Y. Bai, *Nanoscale*, 2023, **15**, 588–598.
77 A. Ahuja, A. Kumar, A. Sengupta, M. Gautam, H. Lohani, P. Kumari and S. Mitra, *Energy Storage Mater.*, 2022, **52**, 169–179.
78 Z. Wu, Y. Zhou, C. Hai, J. Zeng, X. Ren, Y. Sun, Y. Shen, X. Li, S. Dong and G. Zhang, *Ceram. Int.*, 2022, **48**, 17279–17288.
79 Q. Liu, Y. Zhao, W. Liu, M. Wang, J. Ding, Y. Feng, W. You, P. Wang, P. Guan and R. Che, *Nanoscale*, 2019, **11**, 13007–13016.